COMMUNICATIONS

Magnetic Resonance in Medicine 48:577–582 (2002)

High Angular Resolution Diffusion Imaging Reveals Intravoxel White Matter Fiber Heterogeneity

David S. Tuch,[1] Timothy G. Reese,[1] Mette R. Wiegell,[1] Nikos Makris,[2] John W. Belliveau,[1] and Van J. Wedeen[1]*

Magnetic resonance (MR) diffusion tensor imaging (DTI) can resolve the white matter fiber orientation within a voxel provided that the fibers are strongly aligned. However, a given voxel may contain a distribution of fiber orientations due to, for example, intravoxel fiber crossing. The present study sought to test whether a geodesic, high *b*-value diffusion gradient sampling scheme could resolve multiple fiber orientations within a single voxel. In regions of fiber crossing the diffusion signal exhibited multiple local maxima/minima as a function of diffusion gradient orientation, indicating the presence of multiple intravoxel fiber orientations. The multimodality of the observed diffusion signal precluded the standard tensor reconstruction, so instead the diffusion signal was modeled as arising from a discrete mixture of Gaussian diffusion processes in slow exchange, and the underlying mixture of tensors was solved for using a gradient descent scheme. The multitensor reconstruction resolved multiple intravoxel fiber populations corresponding to known fiber anatomy. Magn Reson Med 48:577–582, 2002.

Key words: diffusion; diffusion-weighted MRI (DWI); diffusion tensor imaging (DTI); white matter; tractography

Tissues with regularly ordered microstructure, such as skeletal muscle, spine, tongue, heart, and cerebral white matter, exhibit anisotropic water diffusion due to the alignment of the diffusion compartments in the tissue (1–7). The direction of preferred diffusion, and hence the direction of preferred orientation in the tissue, can be resolved with a method called magnetic resonance (MR) diffusion tensor imaging (DTI) (7), which measures the apparent water self-diffusion tensor under the assumption of Gaussian diffusion. Based on the eigenstructure of the measured diffusion tensor, it is possible to infer the orientation of the diffusion compartments within the voxel so that, for example, the major eigenvector of the diffusion tensor parallels the mean fiber orientation (7), and the minor eigenvector parallels the normal to the mean plane of fiber dispersion (8).

The tensor model is incapable, however, of resolving multiple fiber orientations within an individual voxel. This shortcoming of the tensor model stems from the fact that the tensor possesses only a single orientational maximum, i.e., the major eigenvalue of the diffusion tensor (9,10). At the millimeter-scale resolution typical of DTI, the volume of cerebral white matter containing such intravoxel orientational heterogeneity (IVOH) may be considerable given the widespread divergence and convergence of fascicles (11–13). The abundance of IVOH at the millimeter scale can be further appreciated by considering the ubiquity of oblate (pancake-shaped) diffusion tensors in DTI, a hypothesized indicator of IVOH (3,4,8).

Given the obstacle that IVOH (particularly fiber crossing (14–16)) poses to white matter tractography algorithms (14–20), we sought to determine whether high angular resolution, high *b*-value diffusion gradient sampling could resolve such intravoxel heterogeneity (9). High *b*-values were employed because at the lower *b*-values conventionally employed by DTI there is insufficient contrast between the fast-diffusion component of one fiber and the slow-diffusion component of another fiber to effectively resolve the two fibers (10). Using high angular resolution, high *b*-value diffusion gradient sampling, we were able to detect diffusion signals with multiple, discrete maxima/minima as a function of gradient orientation, indicating the presence of multiple underlying fiber populations. Such IVOH has recently been hypothesized (3,8) to manifest in DTI in the form of oblate diffusion tensors, i.e., diffusion tensors in which the first eigenvalue is comparable to the second, and both are much larger than the third. Here, we found that the non-Gaussianity of the observed diffusion signal (a measure of disagreement with the tensor model) increased with an increase in the oblateness of the measured diffusion tensor. This finding provides preliminary support for the hypothesis that oblate diffusion tensors in DTI arise from IVOH.

The detection of multimodal diffusion signals indicates the presence of IVOH, but it does not resolve the underlying directions of enhanced diffusion. To do so, the diffusion signal was modeled as arising from a discrete mixture of Gaussian diffusion processes in slow exchange (a mixture of tensors). The distribution of tensors within each voxel was solved for using a gradient descent algorithm, which revealed multiple intravoxel fiber orientations corresponding to known fiber anatomy, and consistent with the neighboring fiber anatomy.

[1]Athinoula A. Martinos Center for Biomedical Imaging, Massachusetts General Hospital, Charlestown, Massachusetts.

[2]Center for Morphometric Analysis, Massachusetts General Hospital, Charlestown, Massachusetts.

Grant sponsors: Sol Goldman Charitable Trust; Whitaker Foundation, NIH; AHA.

*Correspondence to: Van J. Wedeen, Athinoula A. Martinos Center for Biomedical Imaging, Massachusetts General Hospital, 149 13th Street, Room 2301, Charlestown, MA 02129. E-mail: van@nmr.mgh.harvard.edu

Received 9 July 2001; revised 15 May 2002; accepted 16 May 2002.

DOI 10.1002/mrm.10268
Published online in Wiley InterScience (www.interscience.wiley.com).

THEORY

Assuming Gaussian diffusion, the diffusion signal from a single diffusion compartment is given by

$$E(\mathbf{q}_k) = \exp(-\mathbf{q}_k{}^T\mathbf{D}\mathbf{q}_k\tau) \quad [1]$$

where $E(\mathbf{q}_k)$ is the normalized diffusion signal magnitude for the diffusion gradient wave-vector $\mathbf{q}_k = \gamma\delta\mathbf{g}_k$, γ is the gyromagnetic ratio, δ is the diffusion gradient duration, $\mathbf{g}_k$ is the kth diffusion gradient, τ is the effective diffusion time, and $\mathbf{D}$ is the apparent diffusion tensor (21,22). To model multiple compartments, if we assume that 1) the inhomogeneity consists of a discrete number of homogeneous regions; 2) the regions are in slow exchange, i.e., separated by a distance much greater than the diffusion mixing length; and 3) the diffusion within each region is Gaussian, i.e., fully described by a tensor, then we can express the diffusion function as a finite mixture of Gaussians

$$E(\mathbf{q}_k) = \sum_j f_j \exp(-\mathbf{q}_k{}^T\mathbf{D}_j\mathbf{q}_k\tau) \quad [2]$$

where f_j is the apparent volume fraction of the voxel with diffusion tensor $\mathbf{D}_j$. The objective then is to find the set of n tensors $\{\mathbf{D}_j\}$ and corresponding volume fractions $\{f_j\}$ that best explain the observed diffusion signal. The Gaussian mixture formulation is convenient because it is capable of describing IVOH, and retains much of the economy of the tensor model.

The traditional method for solving Gaussian mixture problems of this type is the expectation maximization (EM) algorithm (23,24). However, in the present context we needed to solve the mixture problem with physiological constraints on the eigenvalues. Given the inability of the EM algorithm to handle such hard constraints, we employed a gradient descent scheme with multiple restarts to solve the mixture model. The gradient descent algorithm solves for the eigenvectors and volume fractions that give the lowest error between the predicted and observed diffusion signals. The eigenvalues of the individual tensors can be specified a priori or restricted to a particular range in order to prevent the algorithm from overfitting with unphysiological eigenvalues. The details of the mixture model decomposition algorithm employed in this study are described in the Appendix.

METHODS

Data Acquisition

Approval for the study was received from the Massachusetts General Hospital Internal Review Board. A single axial diffusion image of a healthy adult male was taken at 3T (GE Signa) with TR/TE/τ = 2200/140/50 ms, b = 1077 s/mm^2, 8 averages, and 3.125 × 3.125 × 3.1 mm^3 voxels. The diffusion pulse sequence consisted of a twice-refocused balanced echo with a pair of 180° pulses (25). The 180° pulse-pair was situated to minimize eddy current distortions. The gradient (g = 10 mT/m) directions were obtained from the 126 vertices of a fivefold-tessellated icosahedral hemisphere (Fig. 1). For each experiment, images with no diffusion weighting were also obtained in order to normalize for nondiffusion signal attenuation. The signal-to-noise ratio (SNR) was ~65 in the unattenuated image and ~35 in the attenuated image. The total scan time was approximately 40 min.

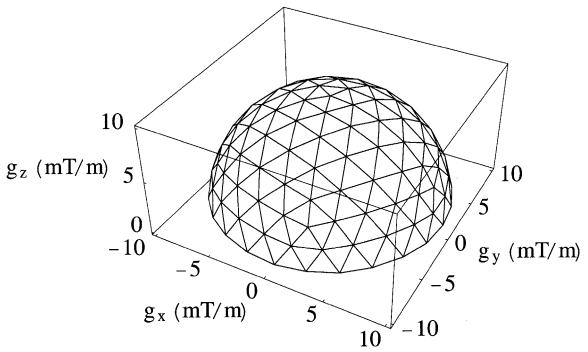

FIG. 1. Gradient directions for the high angular resolution diffusion experiment. The directions were obtained from the 126 vertices of a fivefold-tessellated icosahedral hemisphere.

Model Assessment

The accuracy of the mixture model (Appendix) was assessed by numerical simulation. The simulation considered two fiber populations, each described by a diffusion tensor with eigenvalues $(\lambda_1, \lambda_2, \lambda_3)$ = (1.7, 0.3, 0.3) μm^2/ms. The principal eigenvectors of the two tensors were separated by an angle α. The mixture model reconstruction was then applied using diffusion tensors with eigenvalues $(\lambda_1, \lambda_2, \lambda_3)$ = (1.5, 0.4, 0.4) μm^2/ms. The model eigenvalues and the "true" eigenvalues were deliberately set to different values in order to incorporate the possibility of model misspecification. The mixture model was then solved for varying SNR levels and angular separations α. The accuracy of the reconstruction was defined as the average minimum angle between the reconstructed and "true" principal eigenvectors. The average minimum angle was defined specifically as

$$\theta_{\text{err}} = \frac{1}{N}\sum_{n=1}^{N} \min_m \{\text{acos}[(\hat{\mathbf{e}}_1^n)^T\,\mathbf{e}_1^m]\} \quad [3]$$

where N = 2 is the number of fiber populations, $\hat{\mathbf{e}}_1^n$ is the principal eigenvector of the nth model tensor, and $\mathbf{e}_1^m$ is the principal eigenvector of the mth "true" tensor. The results of the model assessment are shown in Fig. 2.

Data Processing

For each voxel, the mixture model (Appendix) was solved with the conjugate gradient descent algorithm using multiple restarts (six restarts maximum). Multiple restarts were employed to prevent the algorithm from settling on local minima. Approximately half of the iterations found the global minimum. The eigenvalues were specified at $(\lambda_1, \lambda_2, \lambda_3)$ = (1.5, 0.4, 0.4) μm^2/ms based on reported normal values (4). The eigenvalues were preset in order to prevent the individual tensor fits from assuming oblate

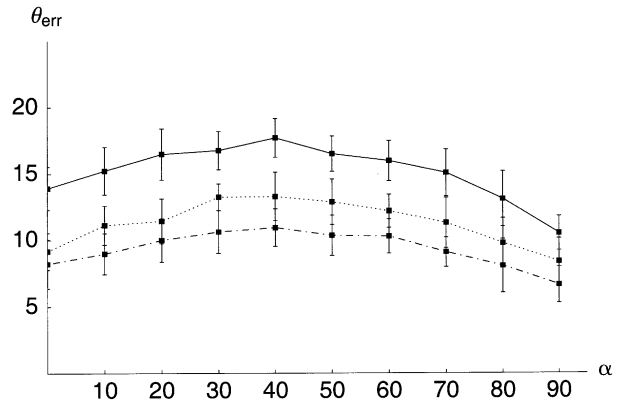

FIG. 2. Numerical simulation results for a two-fiber mixture. The angular error θ_{err} (mean ± SD) between the reconstructed and "true" eigenvectors is plotted as a function of angle α between the "true" eigenvectors. $\alpha = 0°$ corresponds to aligned fibers, and $\alpha = 90°$ corresponds to perpendicular fibers. The simulation was performed for attenuated SNRs of 25 (solid line), 35 (dotted line), and 45 (dash-dotted line) using Gaussian noise. Twenty trials were performed for each α and SNR level.

forms. Alternatively, the eigenvalues could have been treated as model parameters, and physiological values could have been enforced using a softmax transform as was done here with the volume fractions.

If the predicted diffusion signal from a single tensor agreed with the observed diffusion signal with a Pearson correlation coefficient of $\rho > 0.95$, then the number of fibers was set to $N = 1$ and $N = 2$ otherwise. The fits for $N = 3$ fiber populations were found to be unstable in the model simulations, and hence the results from the $N > 2$ fits are not reported. For comparison, single tensor fits were also obtained by the conventional method of applying the *B*-matrix pseudoinverse to the diffusion signals (22).

Data Visualization/Analysis

The raw diffusion data within each voxel were visualized as normalized spherical polar plots of the apparent diffusion coefficient (ADC). The radius of the ADC spherical polar plot function was defined specifically as

$$r(\mathbf{u}) = \frac{1}{Z_1}\log E(\mathbf{u})/Z_2 \qquad [4]$$

where $r(\mathbf{u})$ is the radius of the polar plot as a function of direction u, $E(\mathbf{u})$ is the spin echo signal for direction u, and Z_1 and Z_2 are positive constants that normalize the ADC function to [0,1] within each voxel. It is important to note that the polar plots produced by the above formula are employed only to visualize the raw data—not to resolve the actual directions of enhanced diffusion. Rather, the directions of enhanced diffusion were resolved by the mixture model decomposition.

The results from the mixture model decomposition and the standard diffusion tensor reconstruction were visualized using color-coded cuboid fields. The diffusion tensor (or tensors) within each voxel were rendered as cuboids oriented in the direction of the principal eigenvector of the diffusion tensor. The cuboids were also color-coded according to the direction of the principal eigenvector, with red indicating mediolateral, green anteroposterior, and blue superoinferior.

The non-Gaussianity of the observed diffusion signal within each voxel was compared with the oblateness of the fitted tensor. The non-Gaussianity *W* was defined as the normalized root-mean-square (RMS) difference between the experimentally observed diffusion signals $\mathbf{s}_e$ and the signals $\mathbf{s}_D$ predicted from the single-tensor fit

$$W = \sqrt{\frac{(\mathbf{s}_D - \mathbf{s}_e)^T (\mathbf{s}_D - \mathbf{s}_e)}{\mathbf{s}_e{}^T \mathbf{s}_e}} \qquad [5]$$

The oblateness of the diffusion tensor was expressed as the difference between the second and third eigenvalues, i.e., $\lambda_2 - \lambda_3$ (8).

RESULTS

Diffusion signals exhibiting multiple maxima/minima as a function of gradient orientation were observed in anatomical regions containing fiber crossing and divergence. Specifically, referring to Fig. 3, multimodal diffusion signals were observed where the callosal fibers, turning into the forceps minor, pass the anterior extension of the anterior limb of the internal capsule. Similarly, multimodal diffusion was seen where the fibers diverge into the superior temporal gyrus.

The multitensor decomposition revealed fiber population mixtures that could not be visualized in the original principal eigenvector map (Fig. 4a) or in the ADC function polar plots (Fig. 3). For example, from the anterior limb, the fibers are shown to curve medially to reach the cingulate gyrus, and, with the callosal radiation, diverge laterally into the inferior frontal gyrus, antero-laterally into the middle frontal gyrus, and anteriorly into the superior frontal gyrus (Fig. 4b). Additionally, relative to the tensor model, the mixture estimates gave a stronger antero-posterior course to the anterior limb fibers. The reorientation followed from the ability of the mixture model to account for the medio-lateral fiber component in the callosal striations to the inferior frontal gyrus.

Recently it was proposed that IVOH manifests in DTI in the form of oblate diffusion tensors (3,8), that is, diffusion tensors in which the first eigenvalue is comparable to the second, and both the first and second are significantly larger than the third. To test this hypothesis we compared the non-Gaussianity of the observed diffusion signal (a measure of disagreement with the tensor model) to the oblateness of the measured diffusion tensor. The non-Gaussianity of the diffusion signal was found to increase significantly with the oblateness of the diffusion tensor (Fig. 5), providing support for the hypothesis that oblate diffusion tensors in DTI arise from IVOH.

DISCUSSION AND CONCLUSIONS

Using high angular resolution diffusion imaging, we detected diffusion signals with multiple local extrema as a

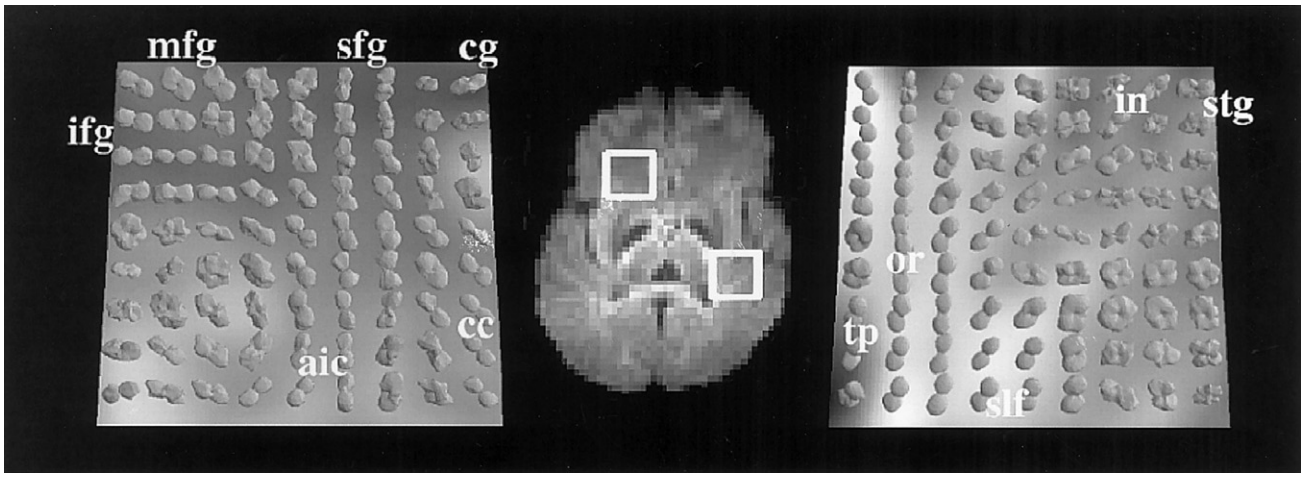

FIG. 3. Spherical polar plots of the ADC function (normalized negative log of the diffusion signal; Eq. [4]) in the fascicle base of the frontal gyri (left), and the divergence of the optic radiation into the superior temporal gyrus (right). The ADC function was rescaled to [0,1] per voxel in order to maximize the visual angular contrast. Note that the peaks of the ADC functions do not give the orientation of the underlying fibers in voxels containing heterogeneity. Multiple peaks simply indicate the presence of IVOH. In the image at left, note the homogeneous diffusion in the corpus callosum (cc), the anterior extension of the anterior limb of the internal capsule (aic), and the projections to the inferior frontal gyrus (ifg). In contrast, multimodal behavior is observed where the fibers diverge into the superior (sfg), middle, and inferior (ifg) frontal gyri, where the fibers curve into the cingulum (cg), and where the fibers from the corpus callosum intersect with those from the anterior internal capsule. At right, homogeneous diffusion is observed in the optic radiation (or), tapetum (tp), and superior longitudinal fascicle (slf), but heterogeneous diffusion is seen where the fibers diverge into the projections to the superior temporal gyrus (stg) and the insula (in).

function of diffusion gradient orientation. The multimodality was apparent primarily in regions of intravoxel fiber crossing and splay, such as at the divergence of fibers to the frontal gyri. Mixture model decomposition of the diffusion signal using a gradient descent algorithm enabled us to resolve the underlying fiber populations that corresponded to known anatomy. Moreover, the mixture decomposition gave fiber angle estimates significantly different from those provided by the tensor model, presumably due to the confounding of the latter by partial volume summation of the multiple underlying fiber directions.

The observation of multimodal diffusion in regions of fiber heterogeneity should raise questions about the general validity of the tensor model. The tensor model is adequate for describing the principal fiber direction in well organized white matter bundles, but may give highly

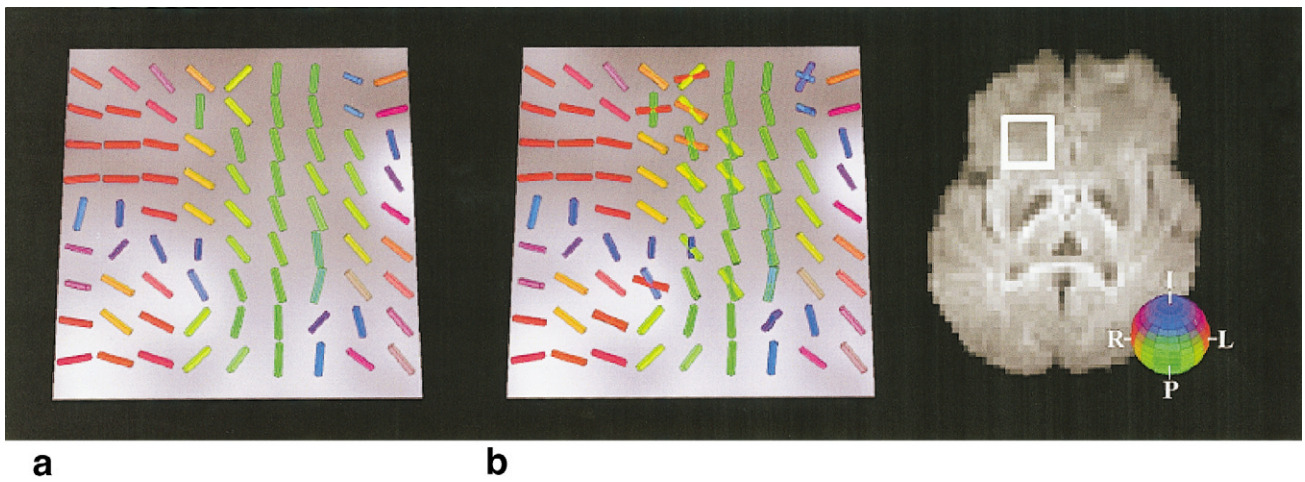

FIG. 4. Comparison of the principal eigenvector fields from the (**a**) single-tensor and (**b**) two-tensor fits to diffusion signal from the forceps minor. The ROI is taken from the same ROI shown in Fig. 3. The vectors are oriented in the direction of the major eigenvector of the diffusion tensor within each voxel and are color-coded according to the RGB sphere shown at right, with red indicating mediolateral, green anteroposterior, and blue superoinferior. **b:** The multitensor decomposition shows the intersections of the lateral and callosal striations with the anterior extension of the anterior limb of the internal capsule; and the divergence of fibers to the superior (bright green), middle (drab green), and inferior (red) frontal gyri. Note also the intersection between the anterolateral directed fibers from the external capsule (bright green), and the superoinferior directed fibers from the uncinate fascicle (blue).

misleading results in regions of fiber heterogeneity. For example, two fibers separated by some angle will give rise to a major eigenvector oriented in between the two underlying fiber orientations—a direction that is inconsistent with either of the underlying fiber orientations. In regions of IVOH, simply taking the negative log of the diffusion signal to obtain the ADC as a function of orientation will not, in general, give a meaningful estimate of the underlying fiber distribution. For example, in Fig. 6, the disagreement between the ADC function polar plot and the fiber directions can be readily appreciated.

For the present study, we employed an arbitrary cut-off in the Pearson correlation coefficient to determine the number of diffusion compartments present. Future work will certainly need to address the question of how many diffusion compartments are present in a more rigorous manner. Such efforts might benefit from the use of more formal model selection approaches, such as information theoretic criteria or cross-validation procedures.

b-Values higher than what are typically used in DTI studies were employed in the present experiment in order to provide sufficient IVOH contrast, a requirement that was recently described in a theoretical report (10). The discrimination power of the mixture model will depend in practice on the *b*-values employed and the details of the reconstruction scheme. In particular, the sensitivity to IVOH will be low at the relatively low *b*-values ($b \approx 700$ s/mm^2) conventionally employed by DTI because there is insufficient contrast between the low-diffusion component from one fiber and the high-diffusion component from another fiber with a different orientation (10). The sensitivity to IVOH will increase with increasing *b*-value, but it will eventually decrease with the associated decrease in SNR. Preliminary data and numerical simulations (unpublished data) suggest that a *b*-value on the order of 1000 s/mm^2 is sufficient for resolving at least two fiber populations, but higher *b*-values will provide greater heterogeneity sensitivity. In general, the optimum sampling scheme will depend on the anisotropy of the underlying fiber populations and the details of the reconstruction algorithm. It would also be worthwhile to examine the resolution power of the various geodesic sampling schemes that have been used in the context of DTI (26,27).

The white matter fascicles comprise approximately a quarter of the total human cerebral white matter volume (11–13). The high angular resolution diffusion imaging method provides a tool for resolving some of the remaining volume of white matter volume (presumably more by fiber number) characterized by complex arrangements of fibers. The present technique promises to directly benefit white matter tractography (14–20), where fiber crossing presents a substantial obstacle (14–16). Specifically, the ability to resolve fiber heterogeneity will allow the tract solutions to navigate through fiber intersections in deep white matter and at the subcortical margin. Furthermore, tract solutions can be initiated in heterogeneous regions, as opposed to the current requirement to initiate the tracts in well-organized fascicles with high anisotropy. Finally, the approach may help characterize selective fiber loss in diseases associated with white matter degeneration.

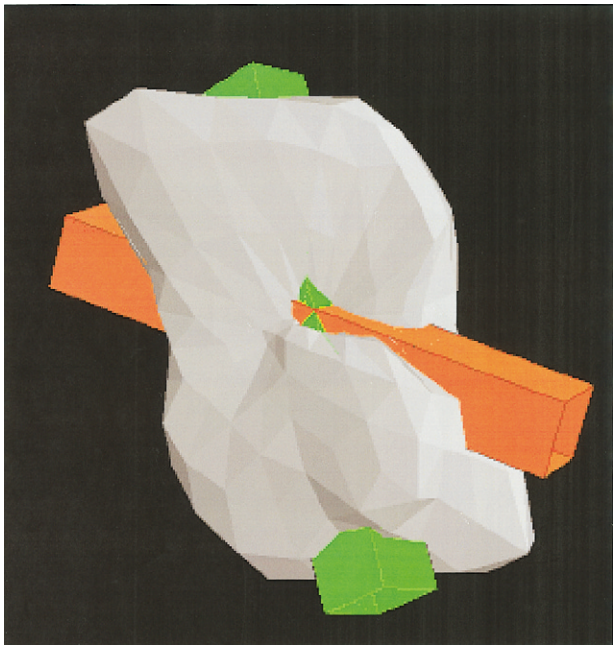

FIG. 6. Single voxel taken from Figs. 3 and 4 at the crossing of the callosal striations with the projections to the superior frontal gyrus. The grayscale polar plot shows the negative log of the diffusion signal as a function of diffusion gradient orientation (the ADC function), and the colored cuboids show the principal eigenvectors of the two tensors that best fit the diffusion signal. Note the disagreement between the direction of the ADC function and the eigenvector estimates.

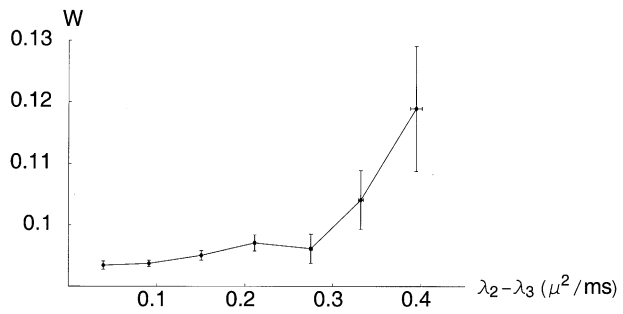

FIG. 5. Experimental relationship between the error *W* (Eq. [5]) of the tensor model and the oblateness metric ($\lambda_2 - \lambda_3$) for the best-fit diffusion tensor. The errors bars are SEM.

ACKNOWLEDGMENTS

This work was supported by the Sol Goldman Charitable Trust (V.J.W.), the Whitaker Foundation (to J.W.B.), the NIH (to J.W.B. and V.J.W.), and the AHA (to J.W.B. and V.J.W.).

APPENDIX

The objective of the mixture model decomposition is to find a set of n tensors $\{\mathbf{D}_j\}$ and corresponding volume fractions $\{f_j\}$ (where $j \in [1,n]$) which best fit the observed diffusion signal $E(\mathbf{q}_k)$ which has been sampled over $\{\mathbf{q}_k\}$. To encourage physiological solutions, we fix the diffusion

tensor eigenvalues to specified values ($\lambda_1, \lambda_2, \lambda_3$). The error function to be minimized is

$$\chi = \sum_k (\hat{E}(\mathbf{q}_k) - E(\mathbf{q}_k))^2 = \sum_k \left(\sum_j f_j \hat{E}_j(\mathbf{q}_k) - E(\mathbf{q}_k) \right)^2 \quad [6]$$

where $\hat{E}$ is the predicted diffusion signal based on the multitensor model, $\hat{E}_j(\mathbf{q}_k)$ is the predicted diffusion signal from compartment j (Eq. [1]), and E is the observed diffusion signal. To ensure that the volume fractions are properly bounded ($f_j \in [0,1]$) and normalized ($\sum_j f_j = 1$) the volume fractions are calculated through the soft-max transform.

$$f_j = \frac{\exp \eta_j}{\sum_i \exp \eta_i} \quad [7]$$

The tensors $\mathbf{D}_j$ are parameterized in terms of the Euler angles α_j^i where $i \in \{1,2,3\}$.

The gradient with respect to the Euler angles is

$$\frac{\partial \chi}{\partial \alpha_j^i} = -\sum_k (\hat{E}(\mathbf{q}_k) - E(\mathbf{q}_k)) f_j \hat{E}_j(\mathbf{q}_k) \mathbf{q}_k^T \left(\frac{\partial \mathbf{R}_j}{\partial \alpha_j^i} \mathbf{\Lambda}_j \mathbf{R}_j^T + \mathbf{R}_j \mathbf{\Lambda}_j \frac{\partial \mathbf{R}_j^T}{\partial \alpha_j^i} \right) \mathbf{q}_k \tau \quad [8]$$

where $\mathbf{R}_j$ is the column matrix of eigenvectors and Λ_j is the diagonal matrix of eigenvalues for tensor $\mathbf{D}_j$. The gradient with respect to the volume fraction parameters is

$$\frac{\partial \chi}{\partial \eta_j} = \frac{\exp \eta_j}{(\sum_i \exp \eta_i)^2} \sum_k [(\hat{E}(\mathbf{q}_k) - E(\mathbf{q}_k)) \sum_i (1 - \delta_{ij}) (\hat{E}_j(\mathbf{q}_k) - \hat{E}_i(\mathbf{q}_k)) \exp \eta_i] \quad [9]$$

where $\delta_{ij} = 1$ if $i = j$, and 0 if $i \neq j$. The mixture model can then be solved by conventional gradient descent methods using the gradients described above.

REFERENCES

1. Cleveland GG, Chang DC, Hazlewood CF. Nuclear magnetic resonance measurements of skeletal muscle. Anisotropy of the diffusion coefficient of the intracellular water. Biophys J 1976;16:1043–1053.
2. Ries M, Jones RA, Dousset V, Moonen CT. Diffusion tensor MRI of the spinal cord. Magn Reson Med 2000;44:884–892.
3. Wedeen VJ, Reese TG, Napadow VJ, Gilbert RJ. Demonstration of primary and secondary muscle fiber architecture of the bovine tongue by diffusion tensor magnetic resonance imaging. Biophys J 2001;80:1024–1028.
4. Pierpaoli C, Jezzard P, Basser PJ, Barnett A, Di Chiro G. Diffusion tensor MR imaging of the human brain. Radiology 1996;201:637–648.
5. Reese TG, Weisskoff RM, Smith RN, Rosen BR, Dinsmore RE, Wedeen VJ. Imaging myocardial fiber architecture in vivo with magnetic resonance. Magn Reson Med 1995;34:786–791.
6. Garrido L, Wedeen VJ, Kwong KK, Spencer UM, Kantor HL. Anisotropy of water diffusion in the myocardium of the rat. Circ Res 1994;74:789–793.
7. Basser PJ, Mattiello J, LeBihan D. MR diffusion tensor spectroscopy and imaging. Biophys J 1994;66:259–267.
8. Wiegell MR, Larsson HB, Wedeen VJ. Fiber crossing in human brain depicted with diffusion tensor MR imaging. Radiology 2000;217:897–903.
9. Tuch DS, Weisskoff RM, Belliveau JW, Wedeen VJ. High angular resolution diffusion imaging of the human brain. In: Proceedings of the 7th Annual Meeting of ISMRM, Philadelphia, 1999. p 321.
10. Alexander AL, Hasan KM, Lazar M, Tsuruda JS, Parker DL. Analysis of partial volume effects in diffusion-tensor MRI. Magn Reson Med 2001; 45:770–780.
11. Meyer JW, Makris N, Bates JF, Caviness VS, Kennedy DN. MRI-based topographic parcellation of human cerebral white matter. Neuroimage 1999;9:1–17.
12. Makris N, Meyer JW, Bates JF, Yeterian EH, Kennedy DN, Caviness VS. MRI-based topographic parcellation of human cerebral white matter and nuclei. II. Rationale and applications with systematics of cerebral connectivity. Neuroimage 1999;9:18–45.
13. Makris N, Worth AJ, Sorensen AG, Papadimitriou GM, Wu O, Reese TG, Wedeen VJ, Davis TL, Stakes JW, Caviness VS, Kaplan E, Rosen BR, Pandya DN, Kennedy DN. Morphometry of in vivo human white matter association pathways with diffusion-weighted magnetic resonance imaging. Ann Neurol 1997;42:951–962.
14. Poupon C, Clark CA, Frouin V, Regis J, Bloch I, Le Bihan D, Mangin J. Regularization of diffusion-based direction maps for the tracking of brain white matter fascicles. Neuroimage 2000;12:184–195.
15. Pierpaoli C, Barnett A, Pajevic S, Chen R, Penix LR, Virta A, Basser P. Water diffusion changes in Wallerian degeneration and their dependence on white matter architecture. Neuroimage 2001;13(6 Pt 1):1174–1185.
16. Basser PJ, Pajevic S, Pierpaoli C, Duda J, Aldroubi A. In vivo fiber tractography using DT-MRI data. Magn Reson Med 2000;44:625–632.
17. Mori S, Kaufmann WE, Pearlson GD, Crain BJ, Stieltjes B, Solaiyappan M, van Zijl PC. In vivo visualization of human neural pathways by magnetic resonance imaging. Ann Neurol 2000;47:412–414.
18. Xue R, van Zijl PC, Crain BJ, Solaiyappan M, Mori S. In vivo three-dimensional reconstruction of rat brain axonal projections by diffusion tensor imaging. Magn Reson Med 1999;42:1123–1127.
19. Mori S, Crain BJ, Chacko VP, van Zijl PC. Three-dimensional tracking of axonal projections in the brain by magnetic resonance imaging. Ann Neurol 1999;45:265–269.
20. Conturo TE, Lori NF, Cull TS, Akbudak E, Snyder AZ, Shimony JS, McKinstry RC, Burton H, Raichle ME. Tracking neuronal fiber pathways in the living human brain. Proc Natl Acad Sci USA 1999;96: 10422–10427.
21. Mattiello J, Basser PJ, Le Bihan D. The b matrix in diffusion tensor echo-planar imaging. Magn Reson Med 1997;37:292–300.
22. Basser PJ, Mattiello J, LeBihan D. Estimation of the effective self-diffusion tensor from the NMR spin echo. J Magn Reson B 1994;103: 247–254.
23. Titterington DM, Smith AFM, Makov UE. Statistical analysis of finite mixture distributions. New York: John Wiley; 1985.
24. Dempster AP, Laird NM, Rubin DB. Maximum likelihood from incomplete data via the EM algorithm. J R Stat Soc B 1977;39:1–38.
25. Reese TG, Weisskoff RM, Wedeen VJ. Diffusion NMR facilitated by a refocused eddy-current EPI pulse sequence. In: Proceedings of the 6th Annual Meeting of ISMRM, Sydney, Australia, 1998. p 663.
26. Jones DK, Simmons A, Williams SC, Horsfield MA. Non-invasive assessment of axonal fiber connectivity in the human brain via diffusion tensor MRI. Magn Reson Med 1999;42:37–41.
27. Skare S, Hedehus M, Moseley ME, Li TQ. Condition number as a measure of noise performance of diffusion tensor data acquisition schemes with MRI. J Magn Reson 2000;147:340–352.